A LETTERS JOURNAL EXPLORING
THE FRONTIERS OF PHYSICS

OFFPRINT

# Electric-field– contact-force– tunable patterns in slipping soft elastic films

DIPANKAR BANDYOPADHYAY, ASHUTOSH SHARMA and V. SHANKAR

EPL, **89** (2010) 36002

A Letters Journal Exploring the Frontiers of Physics

February 2010

EPL, **89** (2010) 36002
doi: 10.1209/0295-5075/89/36002

www.epljournal.org

# Electric-field– and contact-force–induced tunable patterns in slipping soft elastic films

Dipankar Bandyopadhyay[1(a)], Ashutosh Sharma[2(b)] and V. Shankar[2(c)]

[1] *Department of Chemical Engineering, Indian Institute of Technology Guwahati - Guwahati, Assam 781039, India*
[2] *Department of Chemical Engineering, Indian Institute of Technology Kanpur - Kanpur, UP 208016, India*

received 27 November 2009; accepted in final form 18 January 2010
published online 19 February 2010

PACS 68.15.+e – Liquid thin films
PACS 81.16.Rf – Micro- and nanoscale pattern formation
PACS 68.55.-a – Thin film structure and morphology

**Abstract** – We show that the introduction of slippage has a profound effect on instabilities induced by electric field or contact forces in soft solid elastic films. The critical force required to initiate these instabilities is markedly reduced because of slippage, and is lowest when the slippage arises from an intercalating viscous layer between the elastic film and its rigid substrate. Remarkably, unlike in rigidly bonded elastic films, the length scale of instabilities can be tuned by changing the film thicknesses, material properties of the films, and the strength of the destabilizing force of the bilayers. This feature can be potentially exploited in meso-patterning applications.



Elastic contact instabilities [1–9] and electric-field–induced instabilities [10–21] on the surface of a soft elastic film engender self-organized meso-patterns that can be exploited in the micro-fabrication of various components in microelectronics, adhesives and microfluidic devices. A soft elastic film confined either by intersurface forces such as van der Waals or by a field is also a prototype to understand the physics underlying adhesion, delamination, crack propagation, and friction in soft interfaces. Recent studies [1–9] have shown that when a soft elastic film (shear modulus $< 10\,\mathrm{MPa}$) is in contact proximity of a rigid contactor, the intersurface interactions can overcome the restoring elastic and surface tension forces and promote an elastic contact surface instability. The length scale ($\lambda$) of this instability follows the relationship $\lambda = nh$ with the film thickness ($h$) and $n \sim 3$ when the elastic film is thick ($h > 1\,\mu\mathrm{m}$) so that surface energy contributions can be neglected. Instabilities in elastic films could also arise as a result of an applied electric field, and this potentially affords greater control over the destabilizing forces [10–17]. However, previous studies indicate that the soft elastic films deform only under a very high critical voltage [18–20] which may even exceed the dielectric breakdown voltage and thus, it is desirable to accomplish fabrication of patterns under weaker fields. The ability to control the length scale of the patterns is increased in bilayers of elastic films [22–26] when compared to a single film. While previous studies have largely focused on elastic-elastic bilayers, the effect of an intercalating viscous fluid on the patterns has been largely unexplored [27–31]. The presence of a viscous fluid imparts wet-lubrication or an effective slippage to the elastic film (when compared to a rigidly bonded elastic film), and this could potentially decrease the elastic strain energy required to deform the solid film.

In this letter, we demonstrate that slippage induced by a viscous layer underneath the elastic layer (fig. 1) markedly reduces the energy penalty for deformation of the elastic film. The destabilizing force required to initiate instabilities in such bilayers is even smaller than for "dry" slipping films on a rigid substrate. This is because in the case of elastic-viscous bilayers, the free interfaces allow for the possibility of the low-energy bending mode, which is not possible in the case of slipping or rigidly bonded elastic films on a rigid substrate, where only the higher-energy penalty squeezing mode is possible considering the rigid substrate underneath as symmetry plane. We find the dominant length scale of the instability in elastic-viscous (EV) bilayers is a function of the strength of the destabilizing field, compliance of the elastic film and the interfacial tensions at the interfaces, thereby providing an increased ability to tune the length scale of the

(a) E-mail: dipban@iitg.ac.in
(b) E-mail: ashutos@iitk.ac.in
(c) E-mail: vshankar@iitk.ac.in

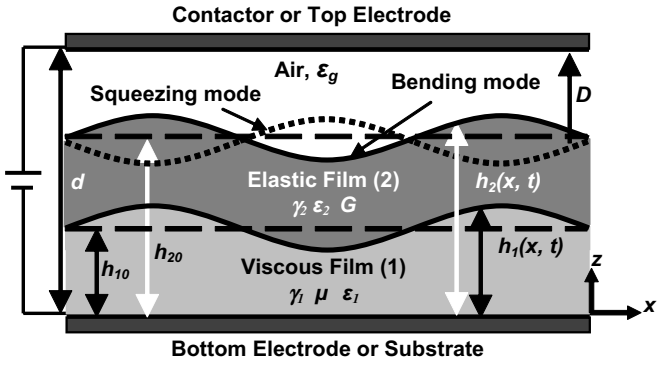


Fig. 1: Schematic diagram of an elastic-viscous bilayer placed on a solid substrate and confined by a contactor. The electric filed is applied through the top and bottom electrodes. The symbols $\gamma_1$ and $\gamma_2$ are the surface energies, $\varepsilon_1$ and $\varepsilon_2$ are the dielectric constants and $\mu$ and $G$ are the viscosity and shear modulus of the viscous and elastic layers. The symbol $d$ is the distance between the electrodes and $D$ is the air gap between the elastic film and the contactor. The solid and the dotted line at the upper interface indicate *squeezing* and *bending* mode of evolution with respect to the solid line at the lower interface.

patterned structures as compared to the rigidly bonded systems.

Figure 1 shows a schematic diagram of an EV bilayer. The presence of two fluid interfaces in bilayers can lead to either in-phase *bending* or anti-phase *squeezing* modes of surface deformations [32]. In the absence of inertia (justified nominally due to the small length scales involved), the following equations of motion and the continuity equation describe the dynamics of incompressible viscous and elastic layer [33]:

$$-\nabla P_1 + \mu\nabla^2\mathbf{v} = 0 \quad \text{and} \quad \nabla\cdot\mathbf{v} = 0, \tag{1}$$

$$-\nabla P_2 + G\nabla^2\mathbf{u} = 0 \quad \text{and} \quad \nabla\cdot\mathbf{u} = 0. \tag{2}$$

Here the subscripts $i = 1$ and 2 denote viscous and elastic layer, respectively. The viscous film is assumed to be perfectly bonded to the rigid substrate ($z = 0$) and therefore, no-slip and impermeability boundary conditions ($\mathbf{v} = 0$) are applied. We apply the continuity of the $x$- and $z$-components of velocities ($\mathbf{v} = \dot{\mathbf{u}}$), the normal stress balance ($\mathbf{n}_1\cdot\boldsymbol{\sigma}_2\cdot\mathbf{n}_1 - \mathbf{n}_1\cdot\boldsymbol{\sigma}_1\cdot\mathbf{n}_1 = \gamma_{21}\kappa_1$), the shear stress balance ($\mathbf{t}_1\cdot\boldsymbol{\sigma}_2\cdot\mathbf{n}_1 = \mathbf{t}_1\cdot\boldsymbol{\sigma}_1\cdot\mathbf{n}_1$) and the kinematic condition ($\dot{h}_1 + (\mathbf{v}\cdot\nabla_s)h_1 = \mathbf{v}\cdot\mathbf{n}_1$) at the elastic-viscous interface ($z = h_1$). At the elastic-air interface ($z = h_2$) the normal stress balance ($\mathbf{n}_2\cdot\boldsymbol{\sigma}_2\cdot\mathbf{n}_2 = -\gamma_2\kappa_2$), the shear stress balance ($\mathbf{t}_2\cdot\boldsymbol{\sigma}_2\cdot\mathbf{n}_2 = 0$) and the kinematic condition ($\dot{h}_2 + (\dot{\mathbf{u}}\cdot\nabla_s)h_2 = \dot{\mathbf{u}}\cdot\mathbf{n}_2$) are enforced. The elastic, viscous and combined film thicknesses are denoted by $h_3$, $h_1$ and $h_2$ ($= h_3 + h_1$), respectively. The respective base state thicknesses are denoted by $h_{30}$, $h_{10}$ and $h_{20}$. The symbols $\mathbf{u}\{u_2^{(x)}, u_2^{(z)}\}$, $\mathbf{v}\{v_1^{(x)}, v_1^{(z)}\}$, $\mathbf{n}_i$, $\mathbf{t}_i$, $\boldsymbol{\sigma}_i$, $\kappa_i$, $P_i(= p_i - \pi_i)$ and $\gamma_i$ are the displacement, velocity, normal, tangent vectors, stress tensor, curvature, non-body force pressure and surface energy of the $i$-th layer, respectively; $p_i$ and $\pi_i$ denote the isotropic pressure and excess pressure due to intermolecular force or electric field; $\mu$, $G$, $\gamma_{21}$, $d$ and $D$ denote viscosity of the liquid layer, shear modulus of the elastic layer, interfacial tension of the elastic-viscous interface [34], distance between the electrodes and the air gap between the elastic film and the contactor, respectively. The superscript dot represents the time derivative of the variable.

We perform a linear stability analysis (LSA) of the bilayer by perturbing with normal linear modes, $\mathbf{v} = \tilde{\mathbf{v}}e^{\omega\, t + \mathbf{i}\, kx}$, $\mathbf{u} = \tilde{\mathbf{u}}e^{\omega\, t + \mathbf{i}\, kx}$, $P_i = \tilde{P}_i e^{\omega\, t + \mathbf{i}\, kx}$ and $h_i = h_{i0} + \tilde{\delta}_i e^{\omega\, t + \mathbf{i}\, kx}$ for any arbitrary wave number $k$ and growth coefficient $\omega$. After eliminating the $\tilde{P}_i$'s we obtain the following biharmonic equations for the liquid and the solid layers:

$$\tilde{v}_1^{\prime\prime\prime\prime(z)} - 2k^2\tilde{v}_1^{\prime\prime(z)} + k^4\tilde{v}_1^{(z)} = 0, \tag{3}$$

$$\tilde{u}_2^{\prime\prime\prime\prime(z)} - 2k^2\tilde{u}_2^{\prime\prime(z)} + k^4\tilde{u}_2^{(z)} = 0. \tag{4}$$

Here the superscript $'$ denotes the derivative with respect to $z$. The general solutions of the ODEs shown in eqs. (3) and (4) are

$$\tilde{v}_1^{(z)} = (A_1 + A_2 z)\exp(kz) + (A_3 + A_4 z)\exp(-kz), \tag{5}$$

$$\tilde{u}_2^{(z)} = (B_1 + B_2 z)\exp(kz) + (B_3 + B_4 z)\exp(-kz). \tag{6}$$

Replacing the expressions for $\tilde{v}_1^{(z)}$, $\tilde{u}_2^{(z)}$, $\tilde{v}_1^{(x)}$, $\tilde{u}_2^{(x)}$, $\tilde{P}_1$ and $\tilde{P}_2$ in the linearized boundary conditions results in a set of eight homogeneous linear algebraic equations involving eight unknown constants $A_i$ and $B_i (i = 1$ to $4)$. Equating the determinant of the coefficient matrix of the set of linear equations to zero, we obtain the general dispersion relation for the EV bilayer. The dominant growth rate ($\omega_m$) and the corresponding wavelength ($\lambda_m$) of instability are obtained from the global maxima of $\omega$ and $\lambda(= 2\pi/k)$. For a more compact representation the dispersion relation is made dimensionless employing, $\beta = h_{30}/h_{10}$, $K = kh_{30}$, $\Gamma_2 = \gamma_2/(Gh_{30})$, $\Omega = \omega\,\mu/G$, $\Gamma_{21} = \gamma_{21}/(Gh_{30})$ and $\Phi_i = \phi_i\, h_{30}/G$, where $\phi_1 = (\partial\pi_1/\partial h_1 - \partial\pi_2/\partial h_1)$, $\phi_2 = (\partial\pi_1/\partial h_2 - \partial\pi_2/\partial h_2)$, $\phi_3 = \partial\pi_2/\partial h_1$ and $\phi_4 = \partial\pi_2/\partial h_2$.

For the contact instabilities, the van der Waals disjoining pressure $\pi_1 = 0$ and $\pi_2 = A/(d - h_2)^3$ are set at the elastic-viscous and elastic-air interfaces, respectively. Here $A$ is the effective Hamaker constant resulting from the interaction between the elastic film and the contactor [34]. The excess pressures at the interfaces resulting from the electric field can be obtained by considering the bilayer as a series capacitor [10–21]. The change in total free energy $\Delta G = -0.5C\psi_b^2$ obtained from the total capacitance ($C^{-1} = C_1^{-1} + C_2^{-1} + C_a^{-1}$) of a series capacitor leads to the expressions for excess electrical

$$\Phi = \frac{[K\{(-2+K\Gamma_{21})(-2+K\Gamma_2)+e^{4K}(2+K\Gamma_{21})(2+K\Gamma_2)-2e^{2K}(4+(8+\Gamma_{21}K^2(-4+\Gamma_2)-4\Gamma_2))\}]}{[-2-2e^{2K}(-4+\Gamma_{21})K+\Gamma_{21}K+e^{4K}(2+K\Gamma_{21})]}. \quad (8)$$

$$\Phi = \frac{[K\{(-1+2BK)(-2+K\Gamma_2)+e^{4K}(1+2BK)(2+K\Gamma_2)-4e^{2K}K^2(-1+(-2+B(-4+\Gamma_2)+\Gamma_2))\}]}{[-1+2BK-4K(1+B)e^{2K}+e^{4K}(1+2BK)]}. \quad (10)$$

pressures ($\pi_1 = \partial(-\Delta G)/\partial h_1$ and $\pi_2 = \partial(-\Delta G)/\partial h_3$) at the interfaces:

$$\pi_1 = \left[\frac{-\varepsilon_0\varepsilon_1\varepsilon_2\psi_b^2\left([\varepsilon_2-\varepsilon_1]+\varepsilon_1\left[1-\varepsilon_2\right]\right)}{2\left[\varepsilon_1\left(h_1+h_3\right)\left[\varepsilon_2-1\right]-h_1\left[\varepsilon_2-\varepsilon_1\right]-\varepsilon_2\varepsilon_1 d\right]^2}\right],$$
$$\pi_2 = \left[\frac{-\varepsilon_0\varepsilon_1^2\varepsilon_2\psi_b^2\left[1-\varepsilon_2\right]}{2\left[\varepsilon_1\left(h_1+h_3\right)\left[\varepsilon_2-1\right]-h_1\left[\varepsilon_2-\varepsilon_1\right]-\varepsilon_2\varepsilon_1 d\right]^2}\right]. \quad (7)$$

The notations $C_1(=\varepsilon_0\varepsilon_1\bar{A}/h_1)$, $C_2(=\varepsilon_0\varepsilon_2\bar{A}/(h_2-h_1))$ and $C_a(=\varepsilon_0\bar{A}/(d-h_2))$ represent the capacitances of the viscous layer, elastic layer and air, respectively. The symbols $\varepsilon_2$, $\varepsilon_1$ and $\varepsilon_0$ represent the dielectric permittivities of the elastic layer, viscous layer and free space; $\bar{A}$ represents the area of the flat interfaces.

The following expression is obtained for a perfect balance of the forces for the contact instabilities of EV bilayers by imposing the neutral stability condition ($\Omega = 0$) to the dispersion relation:

*see eq.* (8) *above*

Here $\Phi = (\partial\pi_2/\partial h_2)\, h_{30}/G$ is a measure of the adhesive force required for deformation. Since the electric-field–induced instabilities in the EV bilayer contain different force components ($\Phi_i = \phi_i\, h_{30}/G$) at the interfaces, we solve the dispersion relation for $\Phi' = [\varepsilon_0\varepsilon_2\psi^2 h_{30}^3(h_{30}/G)]$ after setting $\Omega = 0$. The expression thus obtained [$\Phi' = f(\mathrm{K})$] is cumbersome and not included in this text.

The dispersion relation of the rigidly bonded single elastic film is obtained by setting $h_1 = 0$ [3,5,7,8]:

$$\Phi = K^2\Gamma_2 - 2K\left[1+e^{4K}+2e^{2K}(1+2K^2)\right] \Big/ \left(1-e^{4K}+4Ke^{2K}\right). \quad (9)$$

Linearizing the equations of motion shown in eq. (1) and applying the impermeability and slip boundary condition ($\partial u/\partial z = u/b$) at $z = 0$ and normal and shear stress balance at the elastic-air interface leads to the following dispersion relation for the weakly slipping ($b = h_{30}$) elastic films undergoing contact instability:

*see eq.* (10) *above*

Here $B = b/h_{30}$ and $b$ are the dimensionless and dimensional slip lengths [35–40]. The following dispersion relation of the contact instabilities of strongly or infinitely ($b \to \infty$) slipping elastic films is obtained by applying the free slip boundary condition ($\partial u/\partial z = 0$) at $z = 0$:

$$\Phi = [K\{-2-2e^{2K}(-4+K\Gamma_2)K+\Gamma_2 K + e^{4K}(2+\Gamma_2 K)\}] \Big/ \left(-1+e^{2K}\right)^2. \quad (11)$$

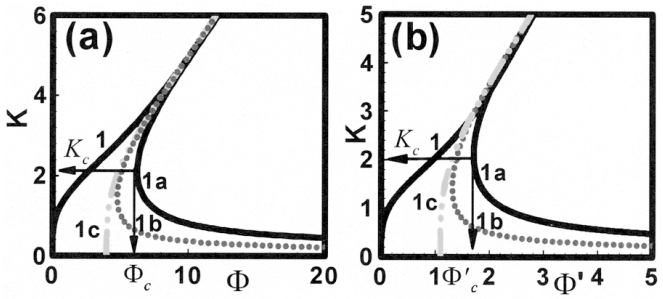


Fig. 2: The plots (a) and (b) show the variations of $\Phi$ and $\Phi'$ with $K$. The curves 1, 1a, 1b and 1c represent elastic-viscous bilayer, rigidly bonded single elastic film, weakly slipping ($b = h_{30}$) and strongly slipping elastic film, respectively. In plot (a) $h_{10} = 1\,\mu$m and in plot (b) $h_{10} = 0.1\,\mu$m. In both the plots $h_{30} = 10\,\mu$m, $\gamma_1 = 0.015\,$N/m, $\gamma_2 = 0.045\,$N/m and $G = 10^6$ Pa.

For rigidly bonded, weakly and strongly slipping single elastic films deforming under electric field the expression $\Phi' = [\varepsilon_0\varepsilon_2\psi^2 h_{30}^3(h_{30}/G)]$ is employed in eqs. (9), (10) and (11) to obtain the neutral stability condition $\Phi' = f(K)$.

It may be noted that the presence of a viscous film (wet-lubrication) introduces a slower time scale for the instability in the EV bilayer compared to the elastic time scale for the case of elastic-film slippage on a dry substrate. In the absence of inertia, the elastic time scale is instantaneous.

In fig. 2 we show the critical force required to initiate the contact instability and electric-field–induced instability in different systems: rigidly bonded elastic films, the EV bilayers with wet lubricating layer, and strongly and weakly slipping elastic films on a dry substrate. Figures 2(a) and (b) show the variations of $\Phi$ and $\Phi'$, respectively, with $K$ for the contact instabilities (electric-field–induced instabilities). The bifurcation diagram (curve 1a) in fig. 2(a) shows that for substrate-bonded elastic films (*i.e.* viscous film thickness, $h_{10} = 0$), the contact instabilities are initiated when the destabilizing force $\Phi$ has magnitude larger than a critical value $\Phi_c$ (minimum of $\Phi$). In contrast, the freely deforming interfaces of the elastic film in the EV bilayers (curve 1) can exhibit instability for any finite positive value of $\Phi$ and have unstable wave numbers extending up to the long-wave regime ($K \to 0$). The bifurcation diagrams for weakly (curve 1b) and strongly (curve 1c) slipping elastic films indicate that $\Phi_c$ is much less for the slipping films than for the rigidly bonded films. However, unlike the EV bilayers, slipping films also deform only beyond a threshold $\Phi$ and even elastic films with infinite slippage

show a finite critical destabilizing force $\Phi_c = 4$ (curve 1c). Interestingly, similar to EV bilayers, the unstable wave numbers for the strongly slipping films (curve 1c) can extend up to the long-wave regime ($K \to 0$) whereas the weakly slipping films (curve 1b) can be unstable for a set of wave numbers with non-zero values, which is like the behavior of rigidly bonded elastic films. Trends similar to these results are also found for electric-field–induced instabilities. Figure 2(b) shows that $\Phi'$ required to initiate the electric-field–induced instabilities is minimum for the EV bilayers (curve 1). The strongly slipping films (curve 1c) require a much lesser $\Phi'_c$ than the weakly slipping films (curve 1b) and the rigidly bonded films (curve 1a) require highest $\Phi'_c$ to exhibit instability. The figure confirms that introduction of slippage reduces the minimum force required to deform an elastic film, which is lowest when the slippage is introduced in the form of a viscous layer under the elastic film. Physically, in case of "dry" slipping or rigidly bonded elastic films the only possible "squeezing mode" of deformation demands larger critical destabilizing force because of the larger strain energy for deformation (defined as the square of the gradient of the displacement field) [9]. In contrast, for EV bilayers, the possibility of the bending mode deformation reduces the critical strain energy for deformation and thus a weaker destabilizing field can deform the solid layer. The curves in fig. 2 also indicate that for longer wavelengths ($k \ll 1$) the critical force requirement is negligible for a bilayer configuration.

The instabilities in the EV bilayers evolve by the selection of the dominant mode with the fastest growth rate. In fig. 3 we show the variation of the dominant growth rate ($\Omega_m$, maximum of $\Omega$) and corresponding wavelength ($\Lambda_m = \lambda_m/h_{30}$) with $H_r$ (ratio of elastic-film thickness to total thickness, $h_{30}/h_{20}$). The intermolecular forces employed to generate in fig. 3 are kept much less than $\Phi_c$ of the rigidly bonded elastic films. Figures 3(a) and (c) show that at low $H_r$, a relatively thick viscous film under the elastic film introduces slip and the instability grows at a faster rate (high $\Omega_m$). With increase in the elastic layer thickness (increase in $H_r$ at constant $h_{10}$) the reduction in the slippage reduces $\Omega_m$. At high $H_r$, the larger deformability of the more compliant ($\sim h_{30}/G$) elastic film leads to a rapid increase in $\Omega_m$. Beyond a threshold thickness of the elastic film, the kinetics of the EV bilayer shows a truly elastic behavior in that $\Omega_m$ diverges to infinity (curve 4 in fig. 3(a)). Further analysis (not presented here) suggests that this curious elastic singularity in $\Omega$ can be regularized by the inclusion of the inertial or dissipative effects in the solid elastic film, as shown elsewhere in a similar context [41,42]. Inclusion of inertia or dissipation leads to very high but finite growth rates. The solid lines in fig. 3(d) suggest that when the viscous film thickness is relatively high (low $H_r$), $\Lambda_m$ is high because of the slippage provided by the thick viscous layer. In contrast, bilayers with thicker elastic films (high $H_r$) show $\Lambda_m \sim 3\,h_{30}$, implying length scales similar to substrate-bonded elastic films [3,5,7,8]. The broken lines

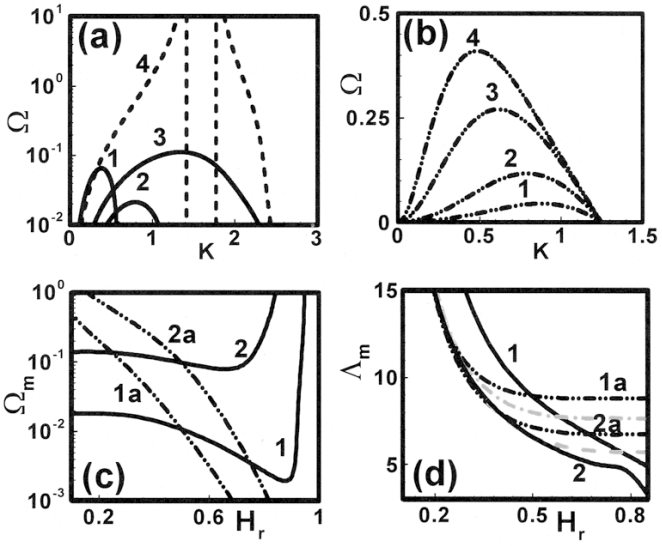


Fig. 3: Plots (a) and (b) show the variation of $\Omega$ with $K$, plots (c) and (d) show the variation of $\Omega_m$ and $\Lambda_m$ with $H_r$. In plot (a) curves 1–4 correspond to $h_{30} = 0.5\,\mu$m, $3.0\,\mu$m, $6.0\,\mu$m and $9.5\,\mu$m, respectively, when $h_{10} = 1.0\,\mu$m. In plot (b) curves 1–4 correspond to $h_{10} = 1.0\,\mu$m, $1.5\,\mu$m, $2.5\,\mu$m, and $3.5\,\mu$m, respectively, when $h_{30} = 1.0\,\mu$m. In plots (c) and (d) solid lines 1 and 2 correspond to $h_{10} = 0.5\,\mu$m and $1.5\,\mu$m and the broken lines 1a and 2a correspond to $h_{30} = 0.5\,\mu$m and $1.5\,\mu$m. The evenly broken gray line in plot (d) corresponds to $G = 5 \times 10^5$ Pa and in the unevenly broken gray line corresponds to $D = 5$ nm. The other parameters in the plots are $\gamma_1 = 0.015$ N/m, $\gamma_2 = 0.045$ N/m, A $= 10^{-20}$ J, $\mu = 1.0$ Pa s, $D = 7.0$ nm and $G = 10^6$ Pa.

in figs. 3(b) and (c) suggest that the influence of slippage is more profound when $h_{30}$ is kept constant and $h_{10}$ is varied as $\Omega_m$ rapidly increases with $h_{10}$. The broken lines in fig. 3(d) suggests that, when $h_{30}$ is constant, $\Lambda_m$ is invariant with change in $h_{10}$ at high $H_r$ because of the negligible effect of slippage. However, at low $H_r$ as the enhanced slippage because of larger $h_{10}$ leads to larger $\Lambda_m$. The evenly and unevenly broken gray lines in fig. 3(d) suggest that reducing $G$ and the air gap $D$ between the contactor and the elastic film can lead to a lowering of $\Lambda_m$.

Much like contact instabilities, EV bilayers can also be unstable under a much weaker electric field as compared to the corresponding rigidly bonded elastic films. In fig. 4, we show the variations of $\Omega_m$ and $\Lambda_m$ with $H_r$. The variable $H_r$ in this figure is obtained by keeping $h_{20}$ constant and varying $h_{30}$ and $h_{10}$. The figure shows two distinct regimes of instabilities: i) a regime dominated by the electric-field force at higher voltages (curves 1 and 1a), and ii) another regime dominated by the slippage at lower voltages (curves 2 and 2a). When the electric field is strong and ($\varepsilon_1 < \varepsilon_2$), curve 1a in fig. 4(a) depicts that $\Omega_m$ increases with increase in $H_r$. The increase in the volume fraction of the elastic film having higher dielectric permittivity increases the strength of the electric field, which eventually increases $\Omega_m$. Similar to the divergence of the growth rate in the contact instability discussed earlier, beyond a threshold

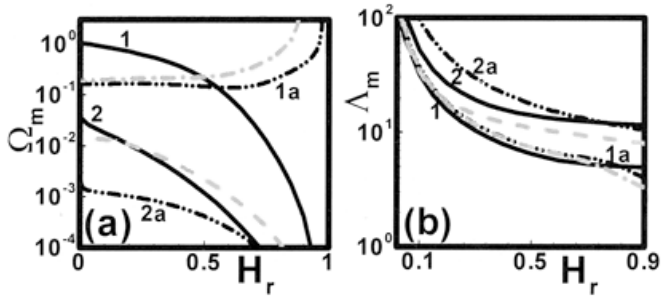


Fig. 4: LSA results for the elastic-viscous bilayer under the influence of an electric field. The solid lines represent $\varepsilon_1(3.0) > \varepsilon_2(2.0)$ and the broken lines represent $\varepsilon_1(2.0) < \varepsilon_2(3.0)$. Plots (a) and (b) show the variations of $\Omega_m$ and $\Lambda_m$ with $H_r$. The curves 1 and 1a correspond to $\psi_b = 200\,\mathrm{V}$; curves 2 and 2a correspond to $\psi_b = 50\,\mathrm{V}$. The evenly broken gray lines correspond to $G = 10^6$ Pa and $\psi_b = 200\,\mathrm{V}$; the unevenly broken gray lines correspond to $D = 50\,\mathrm{nm}$ and $\psi_b = 200\,\mathrm{V}$. The other parameters are $D = 100\,\mathrm{nm}$ ($d = 2.1\,\mu\mathrm{m}$), $\gamma_1 = 0.03\,\mathrm{N/m}$, $\gamma_2 = 0.02\,\mathrm{N/m}$, $h_{20} = 2\,\mu\mathrm{m}$, $\mu = 1.0\,\mathrm{Pa\,s}$ and $G = 10^5$ Pa.

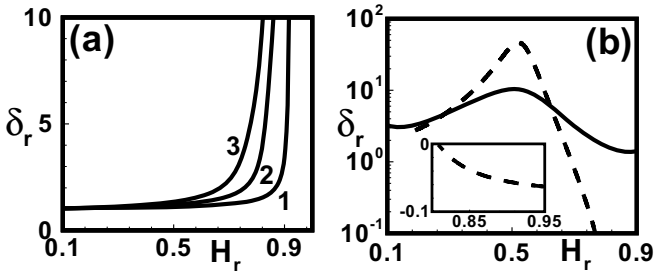


Fig. 5: Plots (a) and (b) show the variation of $\delta_r$ with $H_r$ for the contact instabilities and electric-field–induced instabilities, respectively. In plot (a) curves 1–3 correspond to $h_{10} = 0.5\,\mu\mathrm{m}$, $1.0\,\mu\mathrm{m}$ and $1.5\,\mu\mathrm{m}$, respectively, when $G = 10^6$ and $D = 7.0\,\mathrm{nm}$. In plot (b) the solid lines correspond to $\varepsilon_1(3.0) > \varepsilon_2(2.0)$ and the broken lines correspond to $\varepsilon_1(2.0) < \varepsilon_2(3.0)$. The other parameters are $\psi_b = 200\,\mathrm{V}$, $D = 100\,\mathrm{nm}$ ($d = 2.1\,\mu\mathrm{m}$), $\gamma_1 = 0.03\,\mathrm{N/m}$, $\gamma_2 = 0.02\,\mathrm{N/m}$, $h_{20} = 2\,\mu\mathrm{m}$, $\mu = 1.0\,\mathrm{Pa\,s}$ and $G = 10^5$ Pa.

thickness of the elastic film, the kinetics of instability in this case also diverges. In contrast to curve 1a, curve 1 in fig. 4(a) suggests that when $\varepsilon_1 > \varepsilon_2$ (solid lines), increase in $h_{30}$ (increasing $H_r$) leads to the increase in the volume fraction of the elastic layer having lower dielectric permittivity in the bilayer. Thus $\Omega_m$ progressively reduces as the strength of the electric field reduces. Curves 2 and 2a in fig. 4(a) suggest that at lower voltages, $\Omega_m$ always increases as $H_r$ decreases because of the pronounced influence of the slippage induced by the thicker viscous film underneath the elastic film. Figure 4(b) shows that $\Lambda_m$ always decreases with the progressive increase in $H_r$. The curves suggest that a considerable reduction in $\Lambda_m$ can be obtained by: i) decreasing the shear modulus (curve 1a and evenly broken gray line), ii) decreasing the air gap distance, $D$, between the elastic film and the upper electrode (curve 1a and unevenly broken gray line) and, iii) increasing the voltage (1 and 2). Figures 3 and 4 clearly demonstrate that the length scales of the contact instabilities and the electric-field–induced instabilities of EV bilayers can be tuned by changing the film thicknesses, surface energies, compliance of the elastic film and the intermolecular interaction.

The modes of deformation (squeezing or bending) and the subsequent relative interfacial deformations at the interfaces provide a measure on the quality and type of replication of the patterns generated at one interface to the other. We assume an infinitesimal deformation $\delta_2$ at the elastic-air interface in the $z$-direction, which can be related to the linear displacement $\tilde{u}_z^{(2)} = \tilde{\delta}_2$ at $z = h_2$. In response to this, the $x$- and $z$-component of displacement at $z = h_1$ are assumed as $\tilde{u}_z^{(2)} = \tilde{\delta}_1$ and $\tilde{u}_x^{(2)} = \tilde{\delta}_3$. The sign and the magnitude of $\delta_r (= \tilde{\delta}_2/\tilde{\delta}_1)$, evaluated using $\omega_m$ and $k_m$ from LSA, yield the nature of the fastest deforming mode and the resulting relative amplitudes at the interfaces. A bending mode of deformation results if $\delta_r > 0$ and a squeezing mode ensues if $\delta_r < 0$. Further, the upper (lower) interface deforms more when $|\delta_r| > 1$ ($|\delta_r| < 1$). Figure 5(a) confirms that the contact instabilities at the EV interfaces are always initiated in bending mode ($\delta_r > 1$). It is observed that the deformations at the interfaces are similar ($\delta_r \sim 1$) when the elastic films are less compliant (low $H_r$ or high $G$). More compliant elastic films (high $H_r$ or low $G$) in the bilayers show larger deformation ($\delta_r > 1$) at the elastic-air interface. In contrast to the contact instabilities, the electric-field–induced instabilities can show both squeezing and bending modes of deformations because of the presence of the destabilizing forces at both the interfaces. The broken ($\varepsilon_1 < \varepsilon_2$) and the solid ($\varepsilon_1 > \varepsilon_2$) curves in fig. 5(b) suggest that the bilayers in general show bending mode ($\delta_r > 0$) with larger deformation at the elastic-air interface ($|\delta_r| > 1$). A squeezing mode ($\delta_r < 0$) with a larger deformation at the EV interface ($|\delta_r| < 1$) is only observed when the viscous layer is relatively very thin (high $H_r$) and $\varepsilon_1 < \varepsilon_2$ (inset). Under this condition, a thin viscous layer and a lower resistive interfacial tension allow the elastic-viscous interface to deform towards the substrate and promote instability. The broken line shows that with progressive increase in viscous film thickness, a changeover to bending mode ($\delta_r < 0$) takes place although the deformation at the EV interface still remains higher ($|\delta_r| > 1$). At intermediate $H_r$, when the viscous film is considerably thick, the deformation at the elastic-air interface becomes relatively larger ($|\delta_r| > 1$). Bilayers with thin elastic films (low $H_r$) show similar deformations at both the interfaces ($|\delta_r| \sim 1$).

In summary, we find that the interfacial instabilities in elastic layers confined by van der Waals interactions or electric fields can be greatly modulated by the introduction of slippage, either in the form of dry adhesion/friction or by a viscous sub-layer. The length scales of instabilities in these bilayers are functions of the strength of the destabilizing force, the compliance of the elastic film and the surface energies, thus affording a

greater degree of control on the length scale of instability compared to rigidly bonded or dry slipping elastic films. This control can be potentially useful in applications like micro patterning, pattern replication, etc. Further, thin and hard elastic films exhibit a bending mode with similar amplitude of deformations at both the interfaces, which suggests that these bilayers can be employed for transfer of patterns from one interface (elastic-air) to the other (elastic-viscous) in parallel to generating instability patterns. Most importantly, the EV bilayers deform under a much weaker field than the rigidly bonded elastic films or slipping films because of the possibility of a bending mode of deformation. A much wider range of patterns periodicities and shapes can thus be achieved by changing the viscous film thickness. Interestingly, thick elastic films on very thin viscous films show a length scale similar to that of substrate bonded films with a very rapid "elastic" kinetics of deformation. When the viscous film is thinner than a critical value, the time scale of instability diverges and the inertial and dissipative effects must be included to capture this fast elastic dynamics. Together with earlier studies [41,42], the appearance of a fast elastic time scale in visco-elastic thin film systems that are mostly governed by the viscous time scale, appears to be a generic phenomenon.

* * *

Discussions with Prof. U. Thiele are gratefully acknowledged. AS acknowledges the support of the DST through its grants to the Unit on Nanoscience at IIT Kanpur and an IRHPA grant.

REFERENCES

[1] Ghatak A., Chaudhury M. K., Shenoy V. and Sharma A., *Phys. Rev. Lett.*, **85** (2000) 4329.
[2] Monch W. and Herminghaus S., *Europhys. Lett.*, **53** (2001) 525.
[3] Shenoy V. and Sharma A., *Phys. Rev. Lett.*, **86** (2001) 119.
[4] Ru C. Q., *J. Appl. Phys.*, **90** (2001) 6098.
[5] Shenoy V. and Sharma A., *J. Mech. Phys. Solids*, **50** (2002) 1155.
[6] Ghatak A. and Chaudhury M. K., *Langmuir*, **19** (2003) 2621.
[7] Sarkar J., Shenoy V. and Sharma A., *Phys. Rev. Lett.*, **93** (2004) 018302.
[8] Gonuguntla M., Sharma A., Sarkar J., Subramanian S. A., Ghosh M. and Shenoy V., *Phys. Rev. Lett.*, **97** (2006) 018303.
[9] Gonuguntla M., Sharma A., Mukherjee R. and Subramanian S. A., *Langmuir*, **22** (2006) 7066.
[10] Schäffer E., Thurn-Albrecht T., Russell T. P. and Steiner U., *Nature*, **403** (2000) 874.
[11] Pease III L. F. and Russel W. B., *J. Non-Newtonian Fluid Mech.*, **102** (2002) 233.
[12] Harkema S., Schäffer E., Morariu M. D. and Steiner U., *Langmuir*, **19** (2003) 9714.
[13] Shankar V. and Sharma A., *J. Colloid Interface Sci.*, **274** (2004) 294.
[14] Craster R. V. and Matar O. K., *Phys. Fluids.*, **17** (2005) 032104.
[15] Verma R., Sharma A., Kargupta K. and Bhaumik J., *Langmuir*, **21** (2005) 3710.
[16] Voicu N. E., Harkema S. and Steiner U., *Adv. Funct. Mater.*, **16** (2006) 926.
[17] Li B., Li Y., Xu G. K. and Feng X. Q., *J. Phys.: Condens. Matter*, **21** (2009) 445006.
[18] Arun N., Sharma A., Shenoy V. and Narayan K. S., *Adv. Mater.*, **18** (2006) 660.
[19] Sarkar J., Sharma A. and Shenoy V., *Phys. Rev. E*, **77** (2008) 031604.
[20] Arun N., Sharma A., Pattader P. S. G., Banerjee I., Dixit H. M. and Narayan K., *Phys. Rev. Lett.*, **102** (2009) 254502.
[21] Roberts S. A. and Kumar S., *J. Fluid Mech.*, **631** (2009) 255.
[22] Sarkar J., Sharma A. and Shenoy V., *Phys. Rev. E*, **67** (2003) 031607.
[23] Yoon J., Ru C. Q. and Midouchowski A., *J. Appl. Phys.*, **98** (2005) 113503.
[24] Chung J. Y., Kim K. H., Chaudhury M. K., Sarkar J. and Sharma A., *Eur. Phys. J. E*, **20** (2006) 47.
[25] Tomar G., Sharma A., Shenoy V. and Biswas G., *Phys. Rev. E*, **76** (2007) 011607.
[26] Mukherjee R., Pangule R., Sharma A. and Tomar G., *Adv. Funct. Mater.*, **17** (2007) 2356.
[27] Martin A., Rossier O., Buguin A., Auroy P. and Brochard-Wyart F., *Eur. Phys. J. E*, **74** (2000) 665.
[28] Hosoi A. E. and Mahadevan L., *Phys. Rev. Lett.*, **93** (2004) 137802.
[29] Kumar S. and Matar O. K., *J. Colloid Interface Sci.*, **273** (2004) 581.
[30] Matar O. K., Gkanis V. and Kumar S., *J. Colloid Interface Sci.*, **286** (2005) 319.
[31] Bandyopadhyay D., Sharma A. and Shankar V., *J. Chem. Phys.*, **128** (2008) 154909.
[32] Maldarelli C. H., Jain R. K., Ivanov I. B. and Ruckenstein E., *J. Colloid Interface Sci.*, **78** (1980) 118.
[33] Landau L. D. and Lifshitz E. M., *Theory of Elasticity* (Pergamon Press, London) 1959.
[34] Israelachvili J. N., *Intermolecular and Surface Forces* (Academic Press, London) 1992.
[35] Williams M. B. and Davis S. H., *J. Colloid Interface Sci.*, **90** (1982) 220.
[36] Erneux T. and Davis S. H., *Phys. Fluids A*, **5** (1993) 1117.
[37] Sharma A. and Kargupta K., *Appl. Phys. Lett.*, **83** (2003) 3549.
[38] Kargupta K., Sharma A. and Khanna R., *Langmuir*, **20** (2004) 244.
[39] Fetzer R., Jacobs K., Münch A., Wagner B. and Witelski T. P., *Phys. Rev. Lett.*, **95** (2005) 127801.
[40] Huang S. Q., Li B. and Feng X. Q, *J. Appl. Phys.*, **103** (2008) 083501.
[41] Tomar G., Shankar V., Shukla S. K., Sharma A. and Biswas G., *Eur. Phys. J. E*, **20** (2006) 185.
[42] Tomar G., Shankar V., Sharma A. and Biswas G., *J. Non-Newtonian Fluid Mech.*, **143** (2007) 120.